Optical ice thickness measurement in the VitroJet for time-efficient single particle structure determination

Rene J.M. Henderikx[1,2†*], Saba Shahzad[3,4], Maaike J.G. Schotman[1], Daniel Mann[3,4], Thomas V. Heidler[3,4], Dariush Ashtiani[1], Roger J.M. Jeurissen[5,6], Peter J. Peters[2], Carsten Sachse[3,4,7*], Bart W.A.M.M. Beulen[1†]

[1] CryoSol-World, Weert, The Netherlands
[2] Maastricht Multimodal Molecular Imaging Institute (M4i), Division of Nanoscopy, Maastricht University, Maastricht, The Netherlands
[3] Ernst Ruska-Centre for Microscopy and Spectroscopy with Electrons (ER-C-3): Structural Biology, Forschungszentrum Jülich, Jülich, Germany
[4] Institute of Biological Information Processing (IBI-6): Structural Cell Biology, Forschungszentrum Jülich, Jülich, Germany
[5] ACFD consultancy, Heel, The Netherlands
[6] Physics of Fluids group, University of Twente, Enschede, The Netherlands
[7] Department of Biology, Heinrich-Heine-University, Düsseldorf

[†] These authors contributed equally
* Correspondence should be addressed to: rene.henderikx@cryosol-world.com, c.sachse@fz-juelich.de

Abstract

In cryo-electron microscopy structure determination, embedding biomolecules in vitreous ice of optimal thickness is critical. Ice thickness assessment and selection of suitable holes for data collection are currently part of time-consuming preparatory routines performed on expensive electron microscopes. For this reason, we developed a method to determine ice thickness during sample preparation using the optical camera integrated in the VitroJet. As a result, the ice thickness of buffer-suspended holes on an EM grid can be determined faithfully in the working range relevant for single particle cryo-EM. Dependent on the thickness, the error is below ± 20 nm in the range between 0 - 70 nm down to ± 10 nm in the thinnest ice regions (10 - 40 nm). Single particle structures of apoferritin were determined at two distinct thicknesses of 30 nm and 70 nm to demonstrate the suitability of optical layer thickness measurements for time-efficient cryo-EM structure determination.

1. Introduction

The capabilities of cryogenic electron microscopy (cryo-EM) to determine the structure of biological macromolecules have made tremendous advances in the last decade[1]. The ability to resolve large protein complexes as well as smaller membrane proteins makes it frequently the method of choice for structural biologists[2]. However, to refine atomic models and accurately dock ligands for structure-based drug design, the density maps require details of resolutions better than 3 Å[3,4]. Apart from the molecular particle properties, such as size, structural order and symmetry, ice thickness is a key determinant for the obtainable resolution[5,6]. Ideally, the ice thickness is such that only a monolayer of particles fit into the ice, ensuring full particle hydration and an unobstructed view of the particle in the micrograph. Therefore, the desired ice thickness is dependent on particle dimensions, which typically range from 10 – 100 nm[7]. When the deposited layer is too thin, the particles are not hydrated and often pushed out of the thin areas, while thicker layers add additional noise from the vitreous ice and allow for undesired particle overlap[8]. When collecting data on the protein aldolase with an ideal ice thicknesses of 10 – 20 nm, less than 400 movies were shown to be sufficient to obtain a resolution of 2.8 Å[9]. With the current state of the art cryo-electron microscopes, a data collection of 400 movies only requires around one hour of beam time[10]. The deposition of an optimum sample thickness is experimentally difficult to realize since the influence of sample composition and its fluid properties on the deposition process remains poorly understood[11,12].

In the current cryo-EM workflow, multiple iterations of microscope screening to evaluate sample purity, homogeneity and distribution are common but time-consuming practice[13]. To minimize time required for the identification of the optimal preparation conditions, several studies focused on ice thickness determination in the electron microscope. The principle of this method relies on comparing the intensity of foil holes in presence and absence of an energy filter using the mean free path of the electrons[14,15]. The estimation of ice thickness was demonstrated for different microscope setups and grid types[16–18]. Although these methods help in identifying the optimal grid preparation conditions and targeting holes with suitable ice thickness, the procedure requires additional beam and operator time that is commonly limited.

In grid preparation, classical methods to deposit thin samples rely on pipetting a droplet onto a grid and subsequently wicking away the excess liquid through blotting paper, leaving a thin layer suitable for the penetration of electrons. As this method does not provide accurate control over the liquid removal, variations in thickness from one grid to another and within one grid commonly occur. Consequently, multiple grids need to be screened before finding ice thickness optimal for data acquisition[19]. Alternatives to blotting as a means for sample preparation have been proposed, which can be classified into droplet-spraying and scribing methods. In the droplet-spraying methods, one generates droplets that are sprayed onto the perforated foil of the grid[20–22]. Afterwards, the droplets spread, and in some cases excess sample is wicked away by, for example, nanowires[23]. For scribing methods, a tip moves over the grid and leaves a thin layer of liquid behind [24,25]. Although both new approaches provide an improved control over sample deposition, variations in sample fluid and grid properties still lead to deviations in layer thickness.

In traditional methods, there is no feedback on layer thickness during sample deposition and vitrification. As a result, the quality can only be assessed once the grids are loaded and imaged inside the electron microscope. A few methods that do not involve electron microscopy were put forward to estimate layer thickness based on interference of visible light, either in reflection or transmission[25–27]. In most methods optical intensity is measured as a proxy for ice thickness,

whereas relation between intensity and thickness is unknown. Instead, two studies showed quantification of ice thickness based on the use of neural networks[28,29]. To increase throughput and cost-efficiency, determination of layer thickness during grid preparation would be of great benefit[30].

To obtain the desired layer thickness during grid preparation, we here present a method that estimates the layer thickness in individual holes of the perforated foil from optical images. A camera with on-axis illumination captures images of the grid before and after sample deposition prior to vitrification, and the intensity inside the holes is used to determine the expected ice thickness. We show that the results are in agreement with a theoretical model based on thin layer interferometry. Moreover, we demonstrate that targeted data collection of previously estimated thin areas is beneficial for structure determination of apoferritin. As a result, obtained optical images can minimize the necessary cryo-EM beam time to achieve optimal sample thickness for protein structure resolution.

2. Results

2.1. Camera intensity analysis

2.1.1. Experimental setup

In order to address the challenges of ice thickness optimization using cryo-EM, we set out to characterize on-the-fly imaging capabilities during grid preparation in the VitroJet. Throughout the pin-printing process, a camera integrated in the VitroJet records the sample deposition (Fig. 1A). The light source emits white light, passing through an absorptive and long-pass filter to make the beam uniform and match the transmission range of the objective lens. Using two mirrors and an objective, the light is directed to the autogrid where it interacts with the sample. The reflected light is captured by the objective, and through another mirror imaged by the camera.

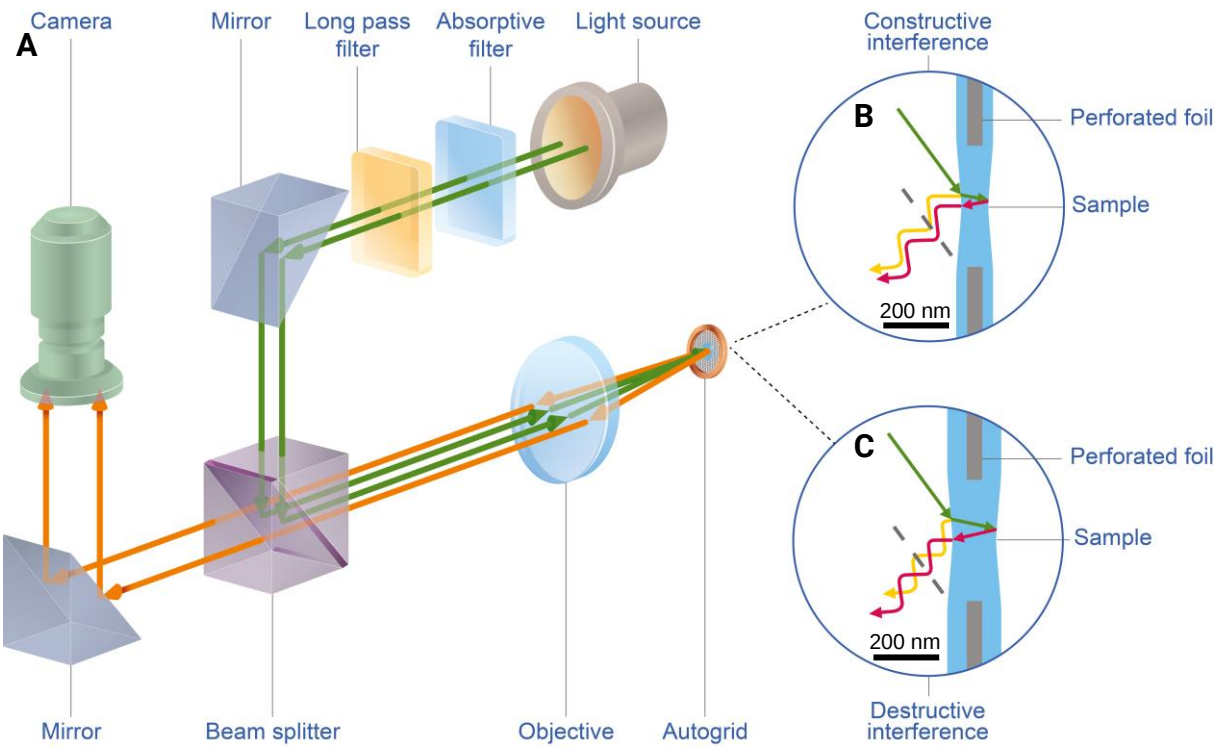

Figure 1 : Schematic overview of the imaging setup integrated in the VitroJet.

(A) White light is generated, passes through filters, a mirror, beam splitter and an objective lens. The light is reflected at the sample and autogrid, passes through the objective again, the beam splitter and another mirror, finally arriving at the camera. Zoomed in sections for thin (B) and thick (C) sample layers indicating how fractions of the light reflect on the first and second air-water interface before vitrification. Depending on the layer thickness, the reflected light will yield constructive or destructive interference.

The light is transmitted or reflected at the both the front and back air-water interface of the sample, where the reflected light wave from different interfaces has an induced phase shift. This leads to a change in total intensity captured by the camera, which is dependent on the specimen thickness (Fig. 1BC). As the layer thickness increases, the reflected intensity will increase until a quarter wavelength of the light is reached, at which constructive interference occurs. Above this thickness, the intensity will decrease again until destructive interference occurs, and Newton interference rings form.

2.1.2. Camera images

Using this setup, images with a field of view of 1.0 x 0.8 mm of the grid before and after deposition are obtained by the camera. The image before deposition shows the mesh of the grid and its perforated foil, including a slight variation in illumination across the field of view (Fig. 2A). Due to the reflection, the appearance of the copper mesh is bright on the image, while the perforated foil is dark. Sample deposition started in the center, and spiraled outwards to cover a circular area with a diameter of approximately 800 µm. The image after deposition shows the grid just before vitrification, where the grey level in the wetted area changed in comparison with the dry grid (Fig 2B, marked with a dashed purple circle). Furthermore, close to the hydrophilic grid bars sample accumulates due to capillary forces, leading to a very thick layer that appears as dark surroundings around each square. Conversely, the center of the squares appears homogeneously bright. The zoomed-in images show that the holes in the foil are clearly detectable (Fig. 2C), including intensity changes due to the deposited sample (Fig. 2D). The difference in intensity depends on layer thickness due to thin film interferometry.

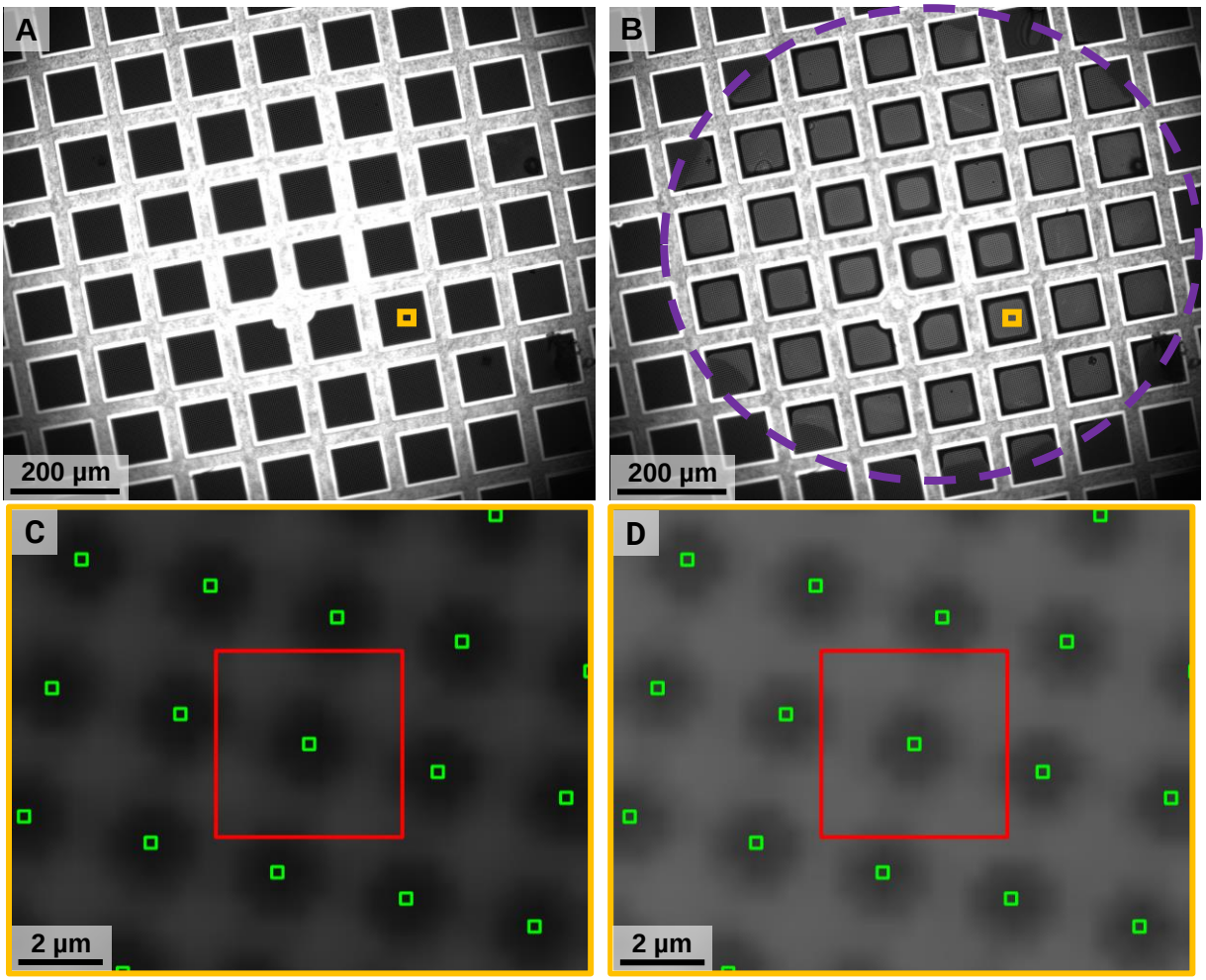

Figure 2: Images acquired by the VitroJet camera before and after sample deposition prior to vitrification.

(A) Image showing the 200 mesh R2/1 grid including the copper mesh and the perforated carbon foil before deposition. (B) Image of the same grid after deposition, where the sample changes the reflected light intensity. The purple dashed circle highlights the area in which deposition by pin-printing occurred. (C and D) Magnified image with bilinear interpolation of A and B, respectively, where the individual holes of the carbon foil are visible. The area used for intensity determination is marked in green, and the region to detect local surrounding carbon intensity in red.

2.1.3. Intensity determination

For quantitative image analysis, the principal grid features can be detected by simple thresholding. First, grid squares are identified based on the brightness and known mesh dimensions. Second, for each square, the dark area close to the grid bars due by sample accumulation are excluded from further analysis by intensity thresholding. In the remaining area within each square, holes are detected using the Hough transform[31]. The circle detection results in an initial estimation of the center of the holes. Due to the small hole size and corresponding limited number of pixels per hole, the center of the holes needs to be refined with sub-pixel accuracy. Therefore, the image is blurred with a kernel of 3 x 3 pixels, and the area around the initial hole location is enlarged ten times using bilinear interpolation. The hole center is determined by the center of mass of the patch of pixels that lies within a range of 30% from the minimum intensity value in the enlarged window. The hole intensity is taken as the mean intensity of a window of 5 x 5 pixels around the center.

Although there are multiple pixels in each detected hole, an empty hole in the image still shows some intensity due to diffraction from the carbon foil and imperfections in the optical system. To compensate for this background signal, the difference between the intensity of each hole before (I_{before}^{hole}) and after deposition (I_{after}^{hole}) was used.

Additionally, the intensity of the light source across the grid is not completely uniform. To correct for this effect, the maximum intensity of the carbon surrounding each individual hole is locally determined (I_{local}^{carbon}). Subsequently, this value is normalized using the maximum carbon intensity in the total field of view (I_{FOV}^{carbon}). In summary, the background corrected intensity for each hole (I^{hole}) is calculated by performing a compensation for the illumination and diffraction according to:

$$I^{hole} = \frac{I_{after}^{hole} - I_{before}^{hole}}{I_{local}^{carbon} / I_{FOV}^{carbon}} \quad (1)$$

2.2. Cryo-EM ice thickness analysis

2.2.1. Electron microscopy images

We exemplify the same grid with images from the electron microscope and subsequently compare it with the obtained optical images. After loading the electron microscope, an atlas of the vitrified grid is recorded with the grid bars and thick ice surrounding the squares appearing dark (Fig. 3A). The grid area outside the deposited area has a speckled appearance due to ice contamination of the perforated foil. The region of the deposited area appears homogeneously grey.

Ice thickness from cryo-EM images is estimated using the energy filter method. For each square, two medium magnification images in the absence and presence of an energy filter are recorded at the same location (Fig. 3BC). Inelastically scattered electrons passing through the sample are removed in the image with the energy filter inserted. The resulting difference in contrast with respect to the non-filtered image can be used to assess ice thickness.

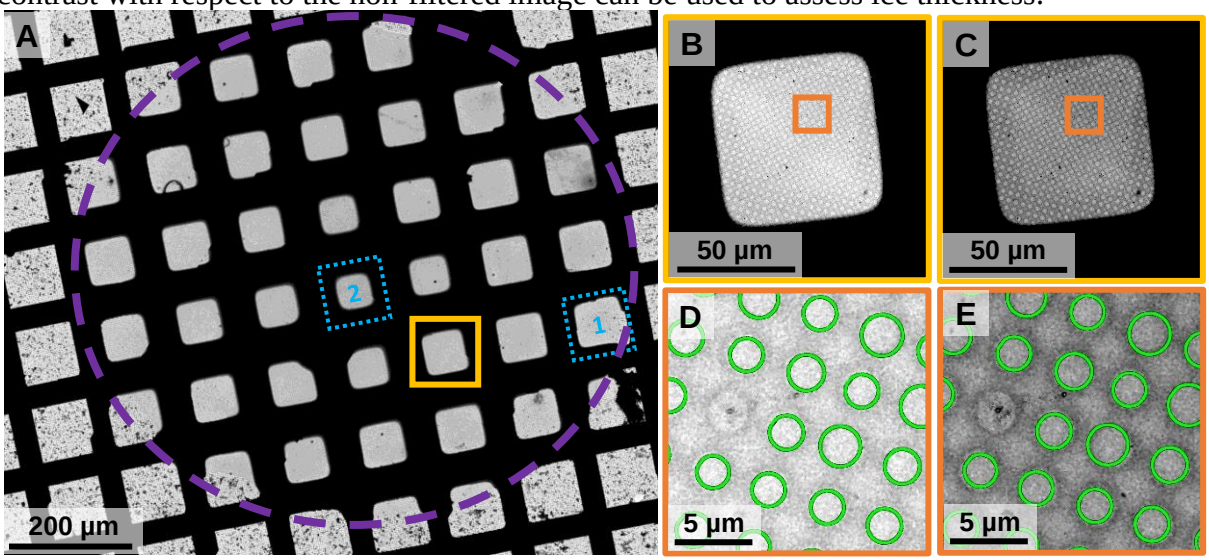

Figure 3: Cryo-EM images after vitrification of the same grid presented in Figure 2.

(A) The low magnification atlas of the grid, showing the spiral deposition pattern in the center of the image, indicated with a dashed purple circle. Data collected for a 3D reconstruction was performed in two squares marked with a dashed blue line. Medium magnification image of the square highlighted in yellow in the atlas (B) without energy filter and (C) with the energy filter

present. Note the increased contrast in the square with the energy filter. (D and E) Enlarged view of the orange area in the medium magnification square image, indicating holes used for analysis in green.

2.2.2. Ice thickness estimation

For each image of the square in absence and presence of the energy filter, the average intensity in each hole is determined (Fig. 3DE). The region close to the grid bars of the square containing thick ice and appearing as a dark ring is excluded from further analysis using intensity thresholding. From the remaining area of the square, the expected number of holes was calculated based on the known grid properties of hole diameter and spacing. Circles with the expected diameter were detected using the Hough transform[31]. Subsequently, false positives were discarded based on implausible distances to nearest neighbors and apparent ice contamination. Subsequently, the average intensity for each hole is determined from a circular area with 15% reduced diameter of the hole size to exclude any carbon edges.

The average intensity in both the unfiltered (I) and the filtered (I_{zl}) image is related to the mean ice thickness (D), as the number of electrons that inelastically scatter in the sample depends on its thickness[14]. Using the apparent mean free path of electrons (λ_{inel}) and the ratio of intensities, the ice thickness can be determined[16]. To ensure that empty holes correspond to a thickness of zero nanometer, a correction factor (C) was introduced[17]:

$$D = \lambda_{inel} \cdot \ln\left(\frac{I}{I_{zl}}\right) - C \qquad (2)$$

In our case, an apparent mean free path of 485 nm is used according to the acceleration voltage of 200 kV and medium magnification during imaging[17]. Although the accuracy for this calibration was not revealed, the variation on the estimated ice thickness is expected to be in the order of 10 % based on mean free path lengths reported in literature[32]. The correction factor is determined by shifting the peak of the empty holes in the histogram to zero by 8.5 nanometer.

2.3. Correlation between intensity and thickness

2.3.1. Spatial correlation

To validate the spatial correlation between optical camera intensity and cryo-EM ice thickness, we inspected the respective grid maps. First, the background corrected intensity from optical camera is plotted over the image after layer deposition (Fig. 4A). Second, the ice thickness is calculated by the energy filter method is superimposed with the cryo-EM atlas (Fig. 4B).

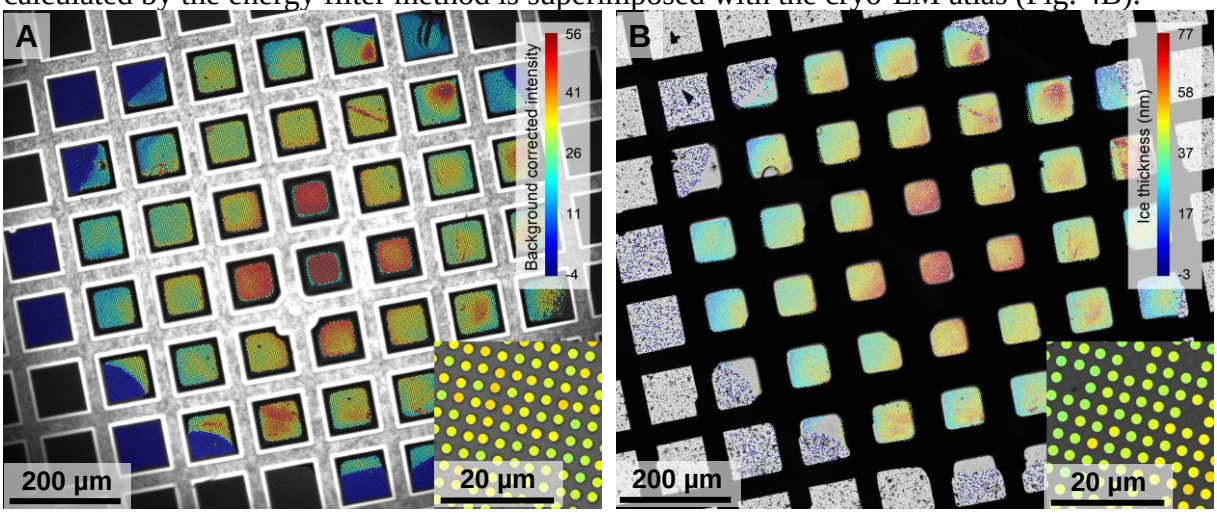

Figure 4: Color overlay of the background corrected intensity from the optical camera, and of the ice thickness measured in the electron microscope on the atlas.

(A) Background corrected intensity overlaid over the optical image of the camera in a color plot. (B) ice thickness with color plot superimposed on cryo-EM atlas obtained in the electron microscope. The matching colors reveal a qualitative correlation between background corrected intensity and ice thickness.

When the holes containing low intensity and ice thickness are colored in the blue, while the bright and thicker ice are colored in red, the spatial distributions of the background corrected intensity and of the ice thickness visually correlate very well. Dark blue colors outside the printing area show that no sample was deposited in these squares. In both color maps, in the deposited region, a gradient can be discerned emanating from center of the grid to the outside rim. Hence, this observation reveals that the optical images instead of energy filtered images may be sufficient for judging optimal ice thickness.

2.3.2. Intensity – thickness correlation

To evaluate the relationship between ice thickness and background corrected intensity from an optical camera quantitatively, a total of 18 grids are analyzed with test specimen apoferritin. Different protocols with distinct printing velocity and standoff distance from pin to grid were used to create layer thicknesses ranging from 0 – 200 nm. To compare holes from the two imaging methods, images must be brought in register using a rigid transformation. After subsequent hole identification and assignment, a total number of 101,673 unique holes with both optical intensity and ice thickness became available and were plotted (Fig. 5A). Two reduced one-dimensional histograms of the data reveal two continuous distributions with most holes corresponding to thinner ice (20 - 50 nm), while there are fewer holes available at larger thickness (Fig. 5BC). An additional peak is found around zero, corresponding to empty holes.

Afterwards, the data pairs are divided into bins of 3 nanometer based on thickness. For each bin, the average and standard deviation of the background corrected intensity was calculated. Subsequently, these values were normalized with the maximum background corrected intensity, which corresponds to the thickness where the reflected light constructively interferes. The average background corrected intensity of each bin is plotted as a function of ice thickness in blue, along with its standard deviation based confidence interval (Fig. 5D).

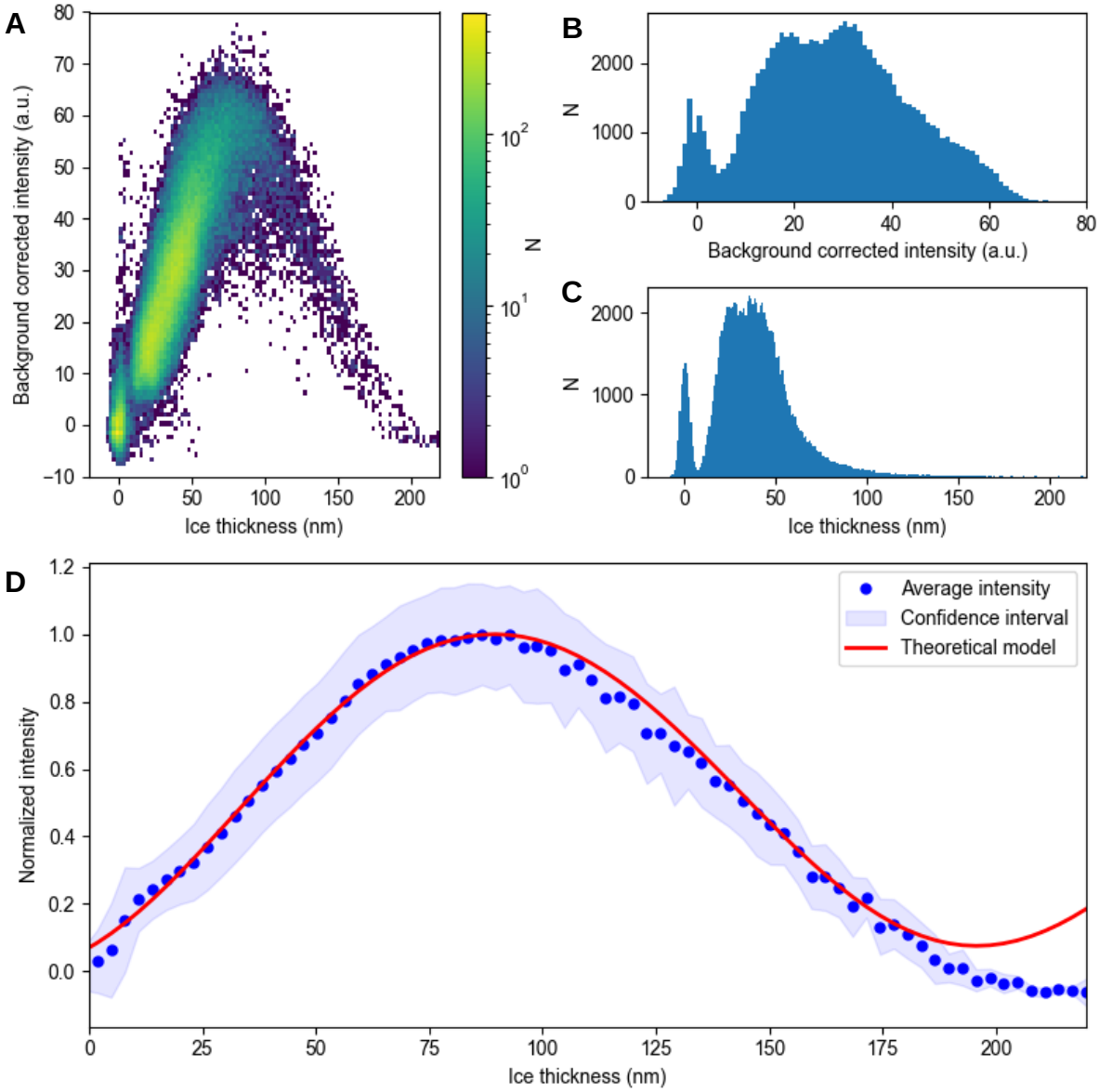

Figure 5: Relationship between optical intensity of VitroJet camera and ice thickness estimation in the microscope.

(A) Scatterplot of identified 101,673 holes with the optical intensity and corresponding ice thickness estimated by the energy filter method, where the number of occurrences for each pixel is indicated by color. Reduced one-dimensional histograms of (B) background corrected intensity and (C) ice thickness. (D) Average background corrected intensity after normalization by the maximum intensity in blue, in combination with the standard deviation presented as confidence intervals. Fit of the theoretical model in red, demonstrating the expected reflectance based on thin film interferometry, matching the experimental data in the 0 – 180 nm interval.

As expected, for empty holes there is no intensity difference in the images before and after deposition, also corresponding to a thickness of zero. At a thickness of around 90 nm, there is a maximum in intensity, which corresponds to constructive interference of the light reflected at the air-water interfaces. At layer thicknesses larger than 90 nm, the intensities decrease down to negative values for destructive interference for thicknesses exceeding 180 nm. Negative values are the consequence of the fact that the carbon foil around these holes also holds a layer

that destructively interferes. Therefore, there is no light diffracting into the holes making the intensity lower than that of the empty grid. Together, a continuous relationship reminiscent of one half of a sine wave dependency exists between image intensities and ice thicknesses from 0 – 180 nm.

2.3.3. Theoretical model

In addition to the measured dependencies, the total amount of light reflected can also be calculated theoretically by thin film interferometry. The reflectance can be determined analytically using equation[33]:

$$R(\lambda, n, t) = \frac{(1-n^2)^2 sin^2(k_o t)}{4n^2 cos^2(k_o t)+(1+n^2)sin^2(k_o t)} \qquad \text{with, } k_0 = 2\pi/\lambda \tag{3}$$

Where R is the reflectance, defined by the ratio between reflected power and incident power, n is the index of refraction, k_0 is the wavenumber of light in free space, λ the wavelength of the light, and t is the layer thickness. Typical refractive index increments for protein solutions are around 0.2 ml/g[34], which would correspond to a change in refractive index of 0.004 for a protein concentration of 20 mg/mL. Therefore, the refractive index of pure water was used in this calculation.

The effective reflectance was determined by calculating the product of the components present in the light path of our setup. These are the incident light, applied filters, camera sensitivity and expected reflectance of the deposited sample. We calculated the effective reflectance as measured with the camera by integrating over the wavelength spectrum:

$$R_{effective}(n, t) = \int R\left(\lambda, n, t - t_{offset}\right) P(\lambda) S(\lambda) T(\lambda) d\lambda \tag{4}$$

Here, $P(\lambda)$ is the intensity of the incident light, $S(\lambda)$ is the camera sensitivity and $T(\lambda)$ the transmission of the applied long pass filter. The theoretical model was fitted with horizontal offset (t_{offset}) of 17 nanometer matching the measured relationship in the plot. The theory and experimental data match up to an ice thickness of 180 nm. When inspecting at the confidence interval of the scatterplot, derived from the standard deviation of the measurements, the accuracy can be put forward. In cases of thin ice (10 - 40 nm), measured intensities can predict the thickness with an error below ± 10 nm. At larger ice thicknesses up to 70 nm, the confidence interval is significantly broader reducing the accuracy to ± 20 nm. The theoretical model based on interferometry follows the relationship between optical intensity and ice thickness with good accuracy for relevant thicknesses used in single particle cryo-EM structure determination. This relationship can therefore be used as a calibration curve for reliable ice thickness estimation based on optical images.

2.4. Single particle structure determination

To demonstrate the relevance of selecting a suitable ice thickness regions for cryo-EM data collection based on optical images, two datasets were acquired on different squares of the previously analyzed grid (See Fig. 3A, dashed blue squares labelled 1 and 2). The average ice thickness of square 1 was optically estimated according to the above established relationship at 30 nm, while square 2 had a thickness of 70 nm (26 nm and 67 nm from the energy filter method, respectively). As expected, the cryo-EM square overview and micrographs show higher contrast at the same defocus when the ice is thinner (Fig 6A-D). For both datasets, the micrographs were processed by motion correction and followed by contrast transfer function

(CTF) estimation (Fig. 6E). The maximum resolutions obtained for fitting the CTF in the thin ice dataset is between 3 – 5 Å, whereas in the thick ice dataset fitting can only be successfully achieved between 5 – 7 Å resulting in poorer accuracy of CTF estimation. A total of 300,000 particles were selected for each dataset and included for a 3D reconstruction of apoferritin (Fig. 6FG). The resolution of the square 1 dataset with thin ice is better at 2.3 Å resolution over 2.5 Å resolution for square 2 with thick ice. When computing structures from subsets of the data and plotting the results in a Rosenthal-Henderson plot[35], the B-factor for both datasets were estimated at 168 and 240 Å^2, respectively (Fig. 6H). Hence, when aiming for 3 Å resolution, only 3967 particles are needed when having thin ice, while using thick ice requires 14,502 particles to reach the same resolution. Effectively one needs 3.7 times less particles and thus microscope time to achieve the same result, in addition to reduced computational resources when analyzing smaller datasets.

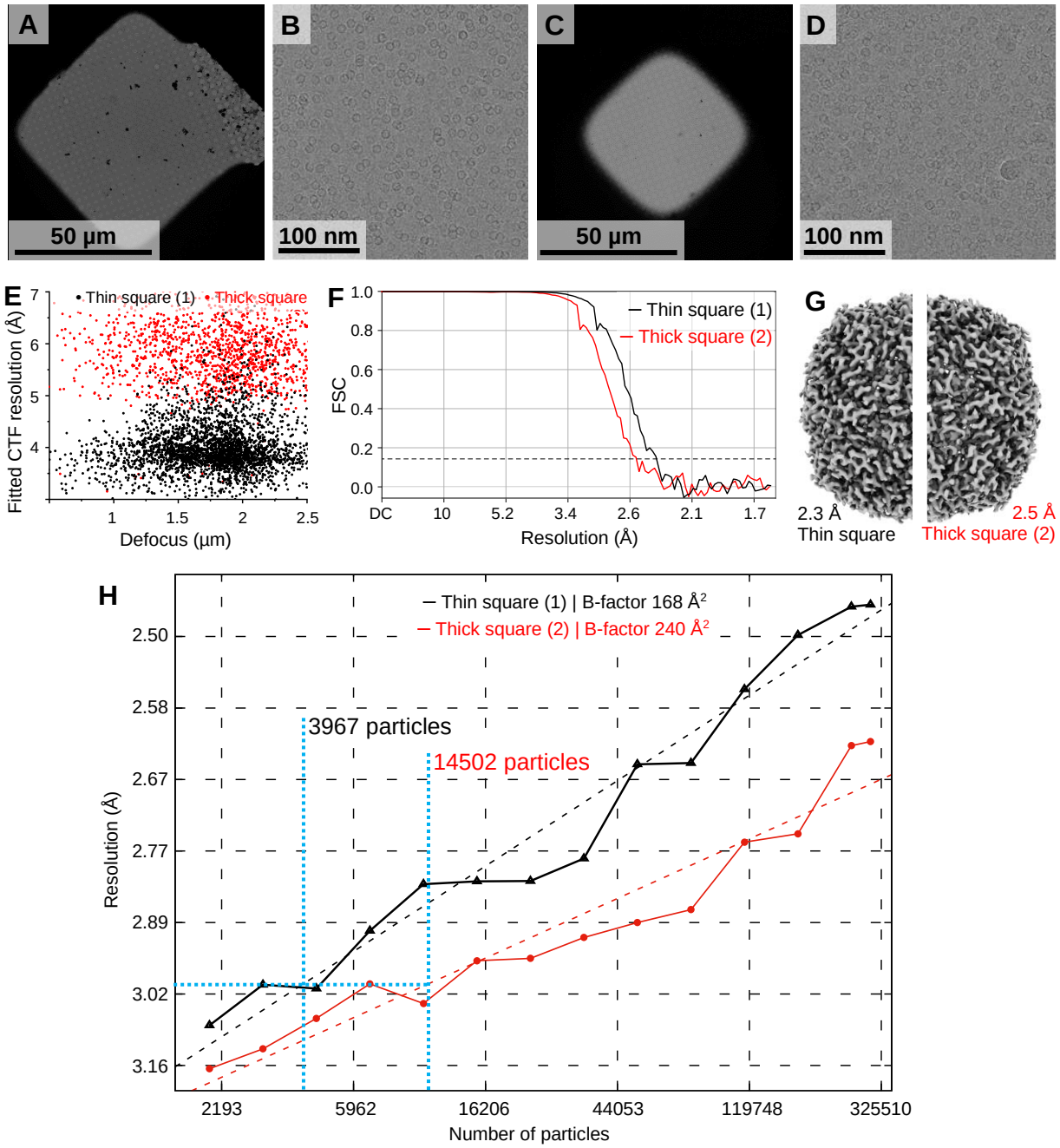

Figure 6: Comparison of two ice thicknesses and their influence on 3D structure determination of apoferritin.

(A) Grid square 1 overview and (B) representative micrograph of apoferritin with thin ice of 30 nm. (C) Grid square 2 overview and (D) representative micrograph of apoferritin with thick ice of 70 nm. Representative micrographs were recorded at the same defocus. Locations of grid squares are marked on the atlas in Figure 3A in dashed blue boxes. (E) Scatterplot of fitted CTF resolution from square 1 (black) and square 2 (red) datasets. High ice thickness limits fitted CTF resolution for the dataset recorded on grid square 2. (F) Fourier shell correlation (FSC) of equally sized batches of 300,000 particles from grid square 1 (black) and 2 (red) selected for structure determination. (G) Reconstructed maps from square 1 (left) and 2 (right) show expected level of detail, e.g., side chain densities, at 2.3 Å and 2.5, respectively. (H) Rosenthal-Henderson plot for square 1 (black) and square 2 (red) datasets. Determined B-factors were calculated at 168 Å^2 and 240 Å^2, respectively. To achieve 3 Å resolution, 3.7 times fewer particles and thus less data collection time is needed for the thin ice sample.

3. Discussion

The results presented in this study demonstrate that ice thickness of individual holes can already be assessed at the stage of sample preparation prior to vitrification. We show that images recorded by the optical camera in the VitroJet can be evaluated with regards to image intensities in holes and correlated with cryo-EM image derived ice thicknesses using the energy filter method (Figures 1 – 4). The optical layer thickness determination is theoretically founded on thin film interferometry, and therefore suitable for predicting ice thicknesses in the range of 0 – 70 nm (Figure 5). Finally, these optically assessed ice thicknesses can be used to select squares of thinner ice resulting in resolution maps with smaller number of particles when compared with particles selected from thicker ice squares (Figure 6).

Thus far, ice thickness determination required the use of an electron microscope[16–18] or a dedicated optical light microscope or camera[25–29]. In our study, the setup integrated in the VitroJet is used, eliminating the need to transfer grids and therefore avoiding potential grid damage and contamination. Additionally, previously presented optical methods provided a thickness prediction on square or atlas level[25–27,29], whereas our method yields an estimation for each individual hole in the perforated foil of the grid. Regarding accuracy of the results, neural network ice thickness prediction has shown to be applicable in a range of 0 – 200 nm with an error of ± 38 nm[28]. Ice thickness estimation in the VitroJet with an analytical model based on thin film interferometry resulted in a smaller applicable range of 0 – 70 nm, but with higher accuracy of ± 20 nm.

Nevertheless, there are several points to be considered when using the optical analysis for ice thickness estimation. The increasing layer thicknesses derived from optical images when plotted showed a clear dependency on the ice thickness following half of a sine wave. Consequently, according to the theory one optical intensity value is represented by multiple ice thicknesses smaller and larger than 90 nm introducing ambiguity for absolute ice thickness determination. Since ice thickness gradients are continuous, the intensities of surrounding holes can be consulted to determine the actual thickness faithfully for relevant ice thicknesses in single particle cryo-EM.

In the theoretical model of layer thickness estimation by interferometry, a negative horizontal offset was observed and compensated for to ensure that the ice thickness will not be

overestimated (Equation 4). There are two factors that may affect the derived relationship between optical layer thickness and cryo-EM ice thickness. Firstly, the optical images are recorded when the sample is still in liquid phase, while the electron microscopy images are taken after the sample is vitrified. In the limited time between the end of deposition and vitrification, the sample is not dewpoint controlled. Redistribution of the liquid on the grid and evaporation during transfer may alter the physical thickness between the two measurement methods. Secondly, the apparent mean free path for the ice thickness estimation using the energy filter method was obtained from reference values, and not calibrated for the used electron microscope. Although one would expect the ice thickness to be directly proportional to the ratio of intensities from filtered and unfiltered image, a negative correction factor had to be applied to shift the thickness of the empty holes to zero nanometer (Equation 2).

The reflection of light is dependent on the index of refraction of the sample, which is known to vary between different samples. The majority of cryo-EM samples are in water-based buffers containing low concentrations of additives, in which the index of refraction will not significantly deviate and thus not influence the layer thickness estimation. Some cryo-EM samples include significant amounts of glycerol, detergents, nanodiscs, liposomes, or are in organic solvents such as branched hydrocarbons, aromatic compounds, esters, ketones, and alcohols, and even strong acids. If the refractive index for these samples is known, it can in principle be taken into account of the theoretical model that converts intensity to expected layer thickness. Samples prepared from non-homogeneous solutions, such as fibrillar amyloid aggregates may require a dedicated calibration on layer thickness.

For reliable prediction of layer thickness, it is important that the holes can be detected from the optical images. Whether the algorithm can successfully detect holes depends on several aspects. First, the hole pattern and foil material are related to the number of pixels per hole and reflectivity around the holes, all of which determine the detectability and accuracy. Second, the grid needs to be sufficiently flat to be in focus over the field of view. Holes that are not exactly in focus will blur the signal over the holes. Moreover, when the foil is not perpendicular to the optical axis, light reflecting outside the objective lens will affect the signal. It is expected that the background correction compensates at least partially for these inaccuracies.

A number of these concerns could be addressed by improving the implementation of the optical setup. When using a monochromatic light source only one wavelength contributes to the signal, simplifying the theoretical model. Since a single wavelength would not convolute the reflection, the range of thicknesses can be expanded and optimum accuracy at the thickness of interest can be achieved. Moreover, the optical system could be improved and a camera with more pixels can be used. Finally, the algorithm to find holes and determine the intensity in holes could be further developed, incorporating details on hole pattern in the hole detection and averaging over multiple frames.

Since frames are recorded from start to end of the deposition, it is possible to monitor the evolution of the layer over time. Using this information, dewpoint settings can be tuned to prevent evaporation or condensation. Additionally, the fluid flow and stability of the sample on the grid during and after deposition can be studied.

The results of this research demonstrate that the layer thickness in individual holes of EM-grids can be determined optically. For single particle cryo-EM, the dimensions of macromolecules are typically in the range between 10 – 100 nm. The measuring accuracy of the cryo-EM ice thickness determination is expected to be in the order of 10 %, while the standard deviation on

the normalized background corrected intensity with the camera is 0.08. Based on the background corrected intensity in optical images, ice thicknesses can be estimated in a range between 0 – 70 nm with an error below ± 20 nm, and with an error below ± 10 nm for the range between 10 - 40 nm. Outside this range, the ice thickness can still be estimated, but the accuracy decreases.

The accuracy of the proposed method is sufficient to allow for on-the-fly tuning of deposition settings to achieve optimal layer thicknesses without the use of an electron microscope. As shown for the test specimen apoferritin, it can significantly decrease elaborate and time-consuming steps to target holes with suitable ice thicknesses during screening. As recording an atlas on a grid takes approximately 10 min, for an autoloader system with 12 grids this results in 2 full hours. If the optical thickness maps are fully transferrable to the electron microscope, in the future it will be possible to skip atlas recording and target most promising grids and holes directly.

4. Materials and methods

4.1. Grids and sample

Copper 200 mesh, carbon R2/1 foil grids (Quantifoil Micro Tools GmbH, Germany) were pre-clipped into an autogrid ring (Thermo Fisher Scientific Inc, MA,l,k USA) at room temperature. Before use, the autogrids were glow discharged in a PELCO easiGlow (Ted Pella Inc., CA, USA) for 60 s at 15 mA, 0.4 mbar including a hold time of 10 seconds. The sample apoferritin from horse spleen was purchased (Sigma-Aldrich / Merck KGaA, Germany), buffer exchanged and concentrated using Amicon Ultra filtration units (Merck KGaA, Germany) to 20 mg/mL in 5 mM Hepes, pH 7.5 and 25 mM NaCl. Aliquots were flash frozen and stored at a temperature of -80 °C before use.

4.2. Grid preparation

To determine the correlation between the camera feedback and ice thickness, the VitroJet (CryoSol-World B.V., The Netherlands) was used to prepare and vitrify grids. Inside the VitroJet, the autogrids were treated using the integrated plasma cleaner for 60 s to ensure reproducible hydrophilicity between grids. Afterwards, the sample was deposited onto the autogrids using pin-printing. In this process, a solid tungsten pin dipped in the pipette to pick up approximately 0.5 nL. Afterwards, the pin approached the foil of the grid to a set standoff distance, such that the sample forms a bridge between pin and grid. A thin layer was deposited by moving the pin laterally to the grid. Deposition started in the center and spiraled out with an interspacing between spirals between 70 - 150 µm to cover a circle with a diameter of 800 µm. The layer thickness is controlled in the VitroJet using the writing velocity and the distance between pin and grid. To create a wide range of layer thicknesses, multiple combinations of velocities 0.5, 1.0 and 2.0 mm/s and standoff distances 10 and 15 µm were used. Sample deposition occurred in a climate chamber with dewpoint at 4 °C. During deposition, both pin and grid were controlled to dewpoint temperature to minimize evaporation. After deposition, the autogrid was vitrified by jet-vitrification. A total of 18 grids were prepared using the VitroJet and imaged both by the optical camera and in cryo-EM.

Sample deposition was monitored by a camera that is integrated in the VitroJet (Fig. 1). The setup had on axis illumination (white LED, SL112, Advanced Illuminations, Vermont, USA) with an absorptive filter and a 495 nm long pass filter (NE20B and FGL495, respectively, Thorlabs GmbH, New Jersey, USA). Light reflected from the grid was captured using a microscope objective (M Plan Apo NIR, 20X, Mitutoyo, USA) and recorded by a camera

(acA2440-20gm, 5MPix, Basler AG, Germany). The images were recorded in real time at a frame rate of 20 fps and stored on a personal computer (HP, USA).

4.3.Cryo-EM analysis

The ice thickness was measured using a Talos Arctica (Thermo Fisher Scientific Inc, MA, USA) operated at 200 kV and equipped with a Gatan K3 camera behind a post-column Bioquantum energy filter (Gatan Inc, CA, USA). Atlas images were acquired at 110 x in LM mode, whereas for recording grid square images, the magnification LM 320 x with a pixel size of 26 nm was chosen. These settings ensured that each image showed exactly one grid square in the field of view. In addition, the intensity was set such that the grid square will receive the final dose of 105 e/pix/s. After setting eucenteric height of the grid square, an unfiltered image of the grid square was recorded. Energy filter with a slit width of 20 eV was inserted. The zero-loss peak manually aligned at the LM magnification before recording a filtered image. This procedure was repeated for those the grid squares that were analyzed with the optical analysis.

Single particle data was recorded on a Titan Krios G4 operated at 300 kV with a non-energy filtered Falcon-IV direct electron detector using EPU software v3.40 (Thermo Fisher Scientific Inc, MA, USA). In the two grid squares with thin and thick ice, 3780 micrographs and 1469 micrographs were recorded, respectively, at a nominal magnification of 96,000x with a calibrated pixel size of 0.808 Å and a total fluence of 30 e^{-}/ Å² in EER mode. A total of 7 exposures per 2 µm hole were acquired with faster beam-tilt acquisition in aberration-free image shift mode with a set defocus between -1.0 and -2.2 µm resulting in approximately 500 images/h. Data processing was performed in CryoSPARC v4.2.1. After patch motion correction with EER upsampling on a 30-frame grid and patch CTF estimation, exposures with a CTF fit worse than 5 Å were excluded for the thin ice square. Particles were picked with ring-shaped blob templates with a 60 Å inner and 110 Å outer diameter and extracted in 256 x 256 pixel squares. These particles were subjected to reference-free 2D classification and classes showing clear secondary structure were selected for further analysis. This subset was used for ab initio 3D map generation with a resolution range of 6 - 9 Å with elevated initial and final batch sizes of 300 and 1000, respectively. Ab initio models were low pass filtered to 12 Å prior to homogeneous 3D refinement with each 300,000 particles with O-symmetry imposed, including local and global CTF refinement (tilt and trefoil), followed by a local non-uniform refinement. ResLog was used to calculate nominal resolutions at FSC = 0.143 for random particle subsets and the final B-factor calculation was performed by linear curve fitting in Gnuplot v6.0. Figures were generated using ChimeraX v1.4 and Adobe Illustrator 2023.

5. References

1. Henderson, R. & Hasnain, S. Cryo-EM': electron cryomicroscopy, cryo electron microscopy or something else? *IUCrJ* **10**, 519–520 (2023).
2. Pandey, A., Shin, K., Patterson, R. E., Liu, X.-Q. & Rainey, J. K. Current strategies for protein production and purification enabling membrane protein structural biology. *Biochem. Cell Biol.* **94**, 507–527 (2016).
3. Subramaniam, S., Earl, L. A., Falconieri, V., Milne, J. L. S. & Egelman, E. H. Resolution advances in cryo-EM enable application to drug discovery. *Curr. Opin. Struct. Biol.* **41**, 194–202 (2016).
4. Scapin, G., Potter, C. S. & Carragher, B. Cryo-EM for Small Molecules Discovery, Design, Understanding, and Application. *Cell Chem. Biol.* **25**, 1318–1325 (2018).
5. Bartesaghi, A. *et al.* 2.2 å resolution cryo-EM structure of β-galactosidase in complex

with a cell-permeant inhibitor. *Science (80-.).* **348**, 1147–1151 (2015).
6. Neselu, K. *et al.* Measuring the effects of ice thickness on resolution in single particle cryo-EM. *J. Struct. Biol. X* **7**, 100085 (2023).
7. Renaud, J.-P. *et al.* Cryo-EM in drug discovery: achievements, limitations and prospects. *Nat. Rev. Drug Discov.* **17**, 471–492 (2018).
8. Kampjut, D., Steiner, J. & Sazanov, L. A. Cryo-EM grid optimization for membrane proteins. *iScience* **24**, 102139 (2021).
9. Kim, L. Y. *et al.* Benchmarking cryo-EM Single Particle Analysis Workflow. *Front. Mol. Biosci.* **5**, (2018).
10. Fréchin, L., Holvec, S., von Loeffelholz, O., Hazemann, I. & Klaholz, B. P. High-resolution cryo-EM performance comparison of two latest-generation cryo electron microscopes on the human ribosome. *J. Struct. Biol.* **215**, 107905 (2023).
11. Glaeser, R. M. *et al.* Factors that Influence the Formation and Stability of Thin, Cryo-EM Specimens. *Biophys. J.* **110**, 749–755 (2016).
12. Weissenberger, G., Henderikx, R. J. M. & Peters, P. J. Understanding the invisible hands of sample preparation for cryo-EM. *Nat. Methods* **18**, 463–471 (2021).
13. Carragher, B. *et al.* Current outcomes when optimizing ‘standard’sample preparation for single-particle cryo-EM. *J. Microsc.* **276**, 39–45 (2019).
14. Grimm, R., Typke, D., Bärmann, M. & Baumeister, W. Determination of the inelastic mean free path in ice by examination of tilted vesicles and automated most probable loss imaging. *Ultramicroscopy* **63**, 169–179 (1996).
15. Brydson, R. *Electron energy loss spectroscopy*. (Garland Science, 2020).
16. Rice, W. J. *et al.* Routine determination of ice thickness for cryo-EM grids. *J. Struct. Biol.* **204**, 38–44 (2018).
17. Rheinberger, J., Oostergetel, G., Resch, G. P. & Paulino, C. Optimized cryo-EM data-acquisition workflow by sample-thickness determination. *Acta Crystallogr. Sect. D* **77**, 565–571 (2021).
18. Hagen, W. J. H. Light ’Em up: Efficient Screening of Gold Foil Grids in Cryo-EM. *Front. Mol. Biosci.* **9**, 912363 (2022).
19. Armstrong, M. *et al.* Microscale fluid behavior during cryo-EM sample blotting. *Biophys. J.* **118**, 708–719 (2020).
20. Dandey, V. P. *et al.* Spotiton: New features and applications. *J. Struct. Biol.* **202**, 161–169 (2018).
21. Kontziampasis, D. *et al.* A cryo-EM grid preparation device for time-resolved structural studies. *IUCrJ* **6**, 1024–1031 (2019).
22. Rubinstein, J. L. *et al.* Shake-it-off: a simple ultrasonic cryo-EM specimen-preparation device. *Acta Crystallogr. Sect. D Struct. Biol.* **75**, 1063–1070 (2019).
23. Wei, H. *et al.* Self-blotting nanowire grids for cryo-EM sample preparation. *Microsc. Microanal.* **23**, 848–849 (2017).
24. Ravelli, R. B. G. *et al.* Cryo-EM structures from sub-nl volumes using pin-printing and jet vitrification. *Nat. Commun.* **11**, 2563 (2020).
25. Arnold, S. A. *et al.* Blotting-free and lossless cryo-electron microscopy grid preparation from nanoliter-sized protein samples and single-cell extracts. *J. Struct. Biol.* **197**, 220–226 (2017).
26. Chua, E. Y. D. *et al.* Vitrocam: A simple low cost Vitrobot camera for assessing grid quality. *bioRxiv* 2006–2022 (2022).
27. Ahn, J. *et al.* Real-time measurement of the liquid amount in cryo-electron microscopy grids using laser diffraction of regular 2-D holes of the grids. *Mol. Cells* **43**, 298 (2020).
28. Last, M. G. F., Voortman, L. M. & Sharp, T. H. Measuring cryo-TEM sample

thickness using reflected light microscopy and machine learning. *J. Struct. Biol.* **215**, 107965 (2023).
29. Hohle, M. M. *et al.* Ice thickness monitoring for cryo-EM grids by interferometry imaging. *Sci. Rep.* **12**, 1–11 (2022).
30. Danev, R., Yanagisawa, H. & Kikkawa, M. Cryo-Electron Microscopy Methodology: Current Aspects and Future Directions. *Trends Biochem. Sci.* **44**, 837–848 (2019).
31. Duda, R. O. & Hart, P. E. Use of the Hough transformation to detect lines and curves in pictures. *Commun. ACM* **15**, 11–15 (1972).
32. Brown, H. G. & Hanssen, E. MeasureIce: accessible on-the-fly measurement of ice thickness in cryo-electron microscopy. *Commun. Biol.* **5**, 817 (2022).
33. Hecht, E. *Optics*. (Pearson Education, Incorporated, 2017).
34. Petsev, D. N., Thomas, B. R., Yau, S.-T. & Vekilov, P. G. Interactions and aggregation of apoferritin molecules in solution: effects of added electrolytes. *Biophys. J.* **78**, 2060–2069 (2000).
35. Rosenthal, P. B. & Henderson, R. Optimal determination of particle orientation, absolute hand, and contrast loss in single-particle electron cryomicroscopy. *J. Mol. Biol.* **333**, 721–745 (2003).

6. Acknowledgements

We are grateful to Raimond Ravelli, Frank Nijpels, Pascal Huysmans & Sanne Thewessem for generating and testing the idea during the prototype phase, and also Giulia Weissenberger for helping in further development. We would like to thank Michiel Peters, Ben Bormans and Bob Ashley for critically reading the manuscript and their helpful feedback. We thank Robin Loose for his contribution to the image analysis algorithm for the electron microscopy images, and Glenn van Kerkvoorde for the schematic overview of the setup. This research received funding from the Netherlands Organization for Scientific Research (NWO) in the framework of the take-off number [17007]. The authors gratefully acknowledge computing time on the supercomputer JURECA [1] at Forschungszentrum Jülich.

[1] Jülich Supercomputing Centre. (2021). JURECA: Data Centric and Booster Modules implementing the Modular Supercomputing Architecture at Jülich Supercomputing Centre Journal of large-scale research facilities, 7, A182. http://dx.doi.org/10.17815/jlsrf-7-182

7. Competing interests

The University of Maastricht filed patents with R.J.M.H., P.J.P. and B.W.A.M.M.B. as inventors regarding sample preparation for cryo-EM. R.J.M.H., M.J.G.S., D.A. and B.W.A.M.M.B. are employed by, and P.J.P. is shareholder of CryoSol-World that holds licenses for these submitted patents. R.J.M.J is a consultant in fluid dynamics for CryoSol-World. S.S., D.M., T.V.H. and C.S. declare that no competing interests exist.